High-Power Directional Emission from Microlasers with Chaotic Resonators

Claire Gmachl, Federico Capasso,* E. E. Narimanov, Jens U. Nöckel, A. Douglas Stone, Jérôme Faist,† Deborah L. Sivco, Alfred Y. Cho

High-power and highly directional semiconductor microcylinder lasers based on an optical resonator with deformed cross section are reported. In the favorable directions of the far-field, a power increase of up to three orders of magnitude over the conventional circularly symmetric lasers was obtained. A "bow-tie"–shaped resonance is responsible for the improved performance of the lasers in the higher range of deformations, in contrast to "whispering-gallery"–type modes of circular and weakly deformed lasers. This resonator design, although demonstrated here in midinfrared quantum-cascade lasers, should be applicable to any laser based on semiconductors or other high–refractive index materials.

Lasers consist of two basic components. First, the active material in which light of a certain wavelength range is generated from an external energy source, such as electric current; second, the laser resonator, which contains the active material, provides feedback for the stimulated emission of light. The resonator largely determines the special features of the emitted light—power, beam directionality, and spectral properties—as well as the laser's physical features such as size and shape. Semiconductor lasers are the most widely used and versatile class of lasers. Their most common resonators are Fabry-Perot cavities, in which two cleaved semiconductor crystal planes act as parallel mirrors, reflecting the light back and forth through the active material.

There have been many attempts to improve resonator properties. In particular, an increase in the reflectivity of the resonator mirrors is highly desirable. This allows low thresholds for the onset of laser action and a smaller volume of active material with concomitant moderate energy requirements and the ability to pack the lasers in a small space.

One excellent example is the development of microdisk semiconductor lasers (*1*). These lasers exploit total internal reflection of light to achieve a mirror reflectivity near unity. Micro-disk, -cylinder, or -droplet lasers form a class of lasers based on circularly symmetric resonators, which lase on "whispering-gallery modes" of the electromagnetic field (*2–4*). In such a mode, light circulates around the curved inner boundary of the resonator, reflecting from the walls of the resonator with an angle of incidence always greater than the critical angle for total internal reflection, thus remaining trapped inside the resonator. There are only minute losses of light caused by evanescent leakage (tunneling) and scattering from surface roughness. This principle allowed the fabrication of the world's smallest lasers (*2*). Besides potential applications in optical computing and networking, microlasers are of strong interest for research problems of cavity quantum electrodynamics, such as resonator-enhanced spontaneous emission and thresholdless lasers (*5*). Small resonators may also serve as model systems for the study of wave phenomena in mesoscopic systems, particularly in the regime where motion is fully or partially chaotic. Recent examples are the quantum mechanics of electrons confined in asymmetric "boxes," such as quantum-dots, stadia, and quantum corrals (*6*), and asymmetric microwave cavities with their strong connection to quantum chaos theory (*7*).

However, as a serious disadvantage, the tiny whispering-gallery–type lasers lack high output power and directional emission because of the high-reflectivity mirrors and the circular symmetry. Attempts to improve this deficiency by making gratings or small indentations on the circumference are so far not very promising (*8, 9*). We now show in experiment and theory how a resonator design that incorporates chaotic ray motion can substantially increase the output power and directionality of such lasers. This effect is demonstrated in semiconductor quantum-cascade lasers emitting in the mid–infrared wavelength region (*10*).

Recent theoretical work has provided insight into the behavior of "asymmetric resonant cavities" (ARCs), whispering-gallery resonators with smooth deformations from cylindrical or spherical symmetry (*11–14*). The ray dynamics in these deformed resonators are either partially or fully chaotic in the generic case (*13*). The best-studied example is a two-dimensional (2D) resonator with a quadrupolar deformation of the circular boundary, described in polar coordinates (r, ϕ) by $r(\phi) \propto [1 + \varepsilon\cdot\cos(2\phi)]$, where ε is the deformation parameter. Partially chaotic whispering-gallery modes in these resonators have shown directional lasing emission in low-index materials (index of refraction $n < 2$, such as glass fibers or cylindrical dye jets) (*12*). The origin of the directional emission is the following (*11*): The deformed boundary causes the angle of incidence of a ray in a whispering-gallery mode to fluctuate in time. Eventually, a ray trapped by total internal reflection impinges on the boundary below the critical angle and escapes by refraction. However, it was not recognized in this earlier theoretical work that, in high-index materials, qualitatively different modes not of the whispering-gallery type might be relevant to the lasing properties.

Here we focus on semiconductor lasers that have an effective index of $n \approx 3.3$ and a deformation of the boundary best described by $r(\phi) \propto [1 + 2\varepsilon\cdot\cos(2\phi)]^{1/2}$, which we will refer to as a "flattened" quadrupole. In general, one can parameterize the boundary of any convex resonator by an arbitrary Fourier series for $r(\phi)$; the above parameterization is chosen for convenience, because it is simply analyzed and describes the actual resonator shapes quite well (Fig. 1). We show that for small deformations ε, the basic picture of chaotic whispering-gallery orbits escaping refractively, as described above, still holds for the high-index semiconductor material. However, we also present strong experimental evidence that at larger deformations a different type of laser resonance emerges and is responsible for highly directional and high-power emission. Unlike the chaotic whispering-gallery modes of smaller deformations, these so-called "bow-tie" resonances are stable resonator modes surrounded on all sides (in phase space) by chaotic motion.

This new class of laser resonators, based on the smooth deformation of a regularly

C. Gmachl, F. Capasso, J. Faist, D. L. Sivco, and A. Y. Cho are at Bell Laboratories, Lucent Technologies, 600 Mountain Avenue, Murray Hill, NJ 07974, USA. E. E. Narimanov and A. D. Stone are in the Department of Applied Physics, Yale University, Post Office Box 208284, New Haven, CT 06520, USA. J. U. Nöckel is at the Max-Planck-Institut fur Physik komplexer Systeme, Nöthnitzer Str. 38, D-01187 Dresden, Germany.

*To whom correspondence should be addressed. E-mail: fc@lucent.com

†Present address: Université de Neuchâtel, rue Bréguet 1, CH-2000 Neuchâtel, Switzerland.

shaped monolithic cavity, is universally applicable to semiconductor lasers or solid-state lasers based on high–refractive index material. It is to some extent related to ring lasers with resonators formed by assembly of several distinct flat or curved mirror surfaces, such as the Ti:sapphire laser (*15*) or optically pumped monolithic solid-state lasers (*16*). We chose the quantum cascade (QC) laser to demonstrate these resonators, because it is particularly suited for 2D whispering-gallery geometries as shown by a recent work on QC microdisk lasers (*17*). It is based on a transition between quantized conduction-band states of a cascaded InGaAs/InAlAs-coupled quantum-well structure (intersubband transition). As such, the selection rule of the optical transition allows light emission only in the 2D plane with polarization normal to the quantum well layers; that is, transverse magnetic (TM) polarization (*18*). Therefore, no light is lost vertical to the laser plane. Furthermore, the QC laser is a unipolar device based only on electron transport, unlike diode lasers. Thus, in contrast to most conventional semiconductor lasers, the surface cannot cause excess unwanted nonradiative recombination of electrons and holes. Finally, the wavelength is comparatively large (several micrometers) and the material used is the well-understood InGaAs/InAlAs system. This choice reduces the importance of roughness (Rayleigh) scattering and makes it easier to fabricate complex shapes.

Device structure and experimental procedure. The lasers are slab-waveguide structures made from a $Ga_{0.47}In_{0.53}As/Al_{0.48}In_{0.52}As$ heterostructure grown by molecular beam epitaxy (MBE) on InP substrate. The waveguide core contains the QC laser active material, designed to emit light of wavelength $\lambda = 5.2$ μm. This active material has been used previously (*19*) and can be considered a mature and optimized design for high-quality laser performance.

The waveguide core is sandwiched between two cladding layers (*20–22*). The entire waveguide is designed to be symmetric and such that the lasing mode (the lowest order TM mode) has almost no (<0.5 %) overlap with the InP substrate. This design prevents possible detrimental effects from light coupling into the substrate.

The cylinder lasers are fabricated by optical lithography and wet chemical etching. The quadrupolar-like shape is obtained starting from a resist pattern that is composed of two semicircles connected by a rectangle (stadium-shape). The samples are then etched until deep mesas are obtained (*23*). Because of the smoothing action of the etchant, the straight section of the etch mask bends toward the curved parts rendering a quadrupole-like shape. Figure 1 shows the top and side view of a laser with deformation $\varepsilon \approx 0.16$. The top view shows that the edge of the resonator follows very well the shape of an exact flattened quadrupole. Ohmic contacts are applied to the front and back surface of the lasers by means of nonalloyed Ti/Au and Ge/Au/Ag/Au, respectively.

Several sets of samples were fabricated. The deformation parameter ε was varied in 10 steps from 0 to ≈0.2. Two different sizes were investigated in order to quantify and rule out size-dependent effects, one with the short diameter ≈50 μm and the long diameter varying from ≈50 ($\varepsilon = 0$) to ≈80 μm ($\varepsilon \approx 0.2$), the second with the short diameter ≈ 30 μm and the long diameter varying from ≈30 to ≈50 μm (*24*). The measurements described below showed that effects arising from the increase in cavity cross section with increasing ε (by less than a factor of 2, for $0 \leq \varepsilon \leq 0.2$) are negligible compared with those introduced by the deformation.

We performed the measurements mainly by contacting the individual cylinder laser with a microprobe in a cryogenically cooled micropositioner stage. To obtain the far-field pattern, we mounted the individual laser on a sample holder that was rotated inside the probe stage. The lasers were driven with current pulses (duration 50 ns, repetition rate ≈40 kHz), and the light output was measured with a cooled HgCdTe detector and a lock-in technique. To improve power output and avoid excess current heating, we recorded the data presented here at 40 to 100 K heat sink temperature. Nevertheless, the maximum pulsed operating temperature of the lasers is 270 K. The spectral properties were measured with a Fourier transform infrared (FTIR) spectrometer.

The lasers emit light according to their symmetry into all quadrants of the 2D laser plane. The experimental set-up did not allow measurement of the spatially integrated power. Therefore, we collected the laser output into an appropriate aperture. Its center angle is varied for the acquisition of the far-field pattern. The light output vertical to the laser plane is broadened by diffraction and was measured integrated over the vertical extension. We introduce a polar coordinate system (r, ϕ) such that $\phi = 0°$

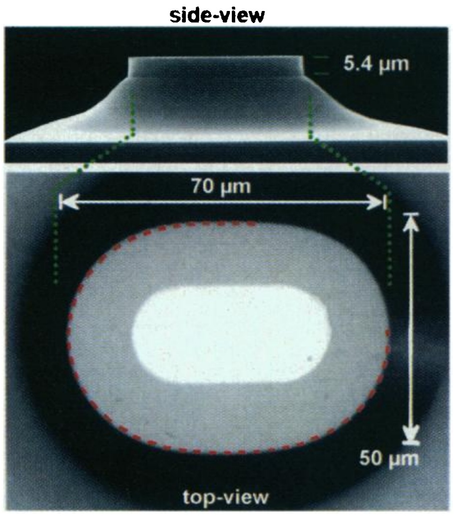

Fig. 1. Scanning electron microscope image of the side and top view of a flattened quadrupolar-shaped cylinder laser. The quadrupolar deformation parameter is $\varepsilon \approx 0.16$. Side view: The laser waveguide and active material is entirely contained in the disk—with vertical side walls, total thickness $d = 5.39$ μm—sitting on a sloped indium-phosphide pedestal. Light emission occurs in the plane of the disk. Top view: The top face of the laser is shown in medium gray, the electric contact in light gray. The laser boundary is very well described by an exact flattened quadrupole with $\varepsilon = 0.16$, which is drawn as dashed red line over the circumference. The boundary of the top electrical contact is approximately parallel to the edge of the cylinder.

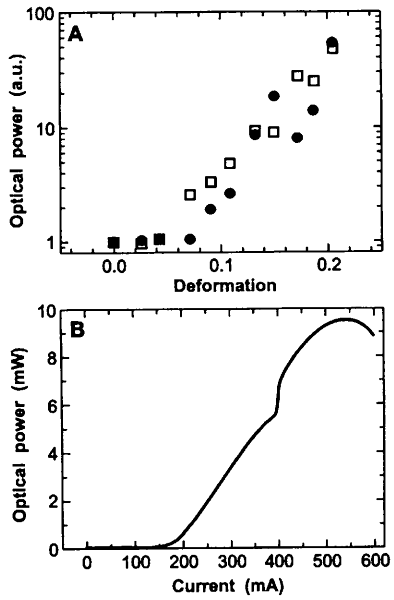

Fig. 2. (**A**) Maximum peak optical power from various lasers as a function of their quadrupolar deformation parameter ε. The aperture with width 15° is centered around zero degrees. Data from two independent sets of lasers are given. The power output is normalized to the power of the respective circular cylinder laser. The scatter of the data is due to the varying number of lasing modes with increasing ε. (**B**) Light output versus current characteristics of a quadrupolar cylinder laser with deformation $\varepsilon \approx 0.2$. The collecting aperture ranges from +40° to +100° (the polar coordinate system is described in the text and in Fig. 3C). The kink around 400 mA indicates the onset of a second lasing mode. The measurement was performed at 100 K heat-sink temperature. The lasers were tested up to 270 K.

indicates the direction along the elongated (major) axis. Accordingly, $\phi = 90°$ denotes the direction of the compressed (minor) axis. Hence, a measurement taken at $\phi = 0°$ has the detector facing one point of highest curvature of the deformed laser.

Power output and beam directionality. The deformed cylinder lasers provided a substantial increase both of the emitted power and directionality (Figs. 2 and 3).

Light output measurements for various lasers as a function of their deformation ε are shown in Fig. 2A. To generate this plot, we recorded the maximum obtainable peak power for each laser by optimizing the pulsed drive current (*25*). The collecting aperture (slit width corresponding to $\approx 15°$) was oriented around $\phi = 0°$. This set-up precludes the observation of any changes in the far-field directionality with deformation. Similar measurements were performed with the aperture oriented around $\phi = 45°$ and $\phi = 90°$. The striking result is the strong (quasi-exponential) increase of the collected optical power with deformation. For the largest deformation under consideration ($\varepsilon \approx 0.2$), a power increase by a factor of ≈ 50 with respect to the circular case is observed. Figure 2A shows a representative measurement taken at $\phi = 0°$.

We measured the absolute output power in some highly deformed laser devices by bonding and mounting them in a calibrated set-up usually used with Fabry-Perot–type lasers. One example, obtained from a laser with $\varepsilon \approx 0.2$, is shown in Fig. 2B. The light-collecting aperture was increased to its maximum size, and the sample was tilted to detect roughly the optical power in an angle from $+40°$ to $+100°$. The choice of this aperture, which exploits far-field anisotropy, will become clear below. A peak output power of ≈ 10 mW at 100 K was obtained. This value is about three orders of magnitude greater than that obtained from the nondeformed (circular cylindrical) laser or previous conventional circular QC-disk lasers (*17*). For a weakly deformed laser ($\varepsilon = 0.06$), we estimate a peak power output of ≈ 50 μW (when measured with comparable collection efficiency as in the laser of Fig. 2B).

A quasi-exponential increase of the collected power with increasing deformation (similar to the one shown in Fig. 2A) has been measured in numerous sets of lasers of various—flattened and less flattened—quadrupolar shapes and sizes, and with various orientations of the aperture. Thus, it appears that the power increase is a reliable, universal effect. However, the increase in output power per unit angle is closely entangled with the actual variation of the far-field pattern with deformation. Indeed, in our lasers the power increase with deformation results from the lasing of different types of modes in different ranges of ε. There is a crossover at intermediate deformations ($\varepsilon \approx 0.12$) from emission via whispering-gallery modes, which dominates at smaller deformations, to laser emission from bow-tie modes, which do not exist below $\varepsilon \approx 0.10$ but dominate the high-deformation regime.

In addition to the strong increase in power output, the deformed lasers can also provide strong directionality. The results of the far-field measurements are summarized in Fig. 3, A and C. As expected, the circular cylinder laser displays no directionality of the emission. At small deformations ($\varepsilon \leq 0.10$), the far-field is only weakly structured with an increased emission in direction of the minor axis com-

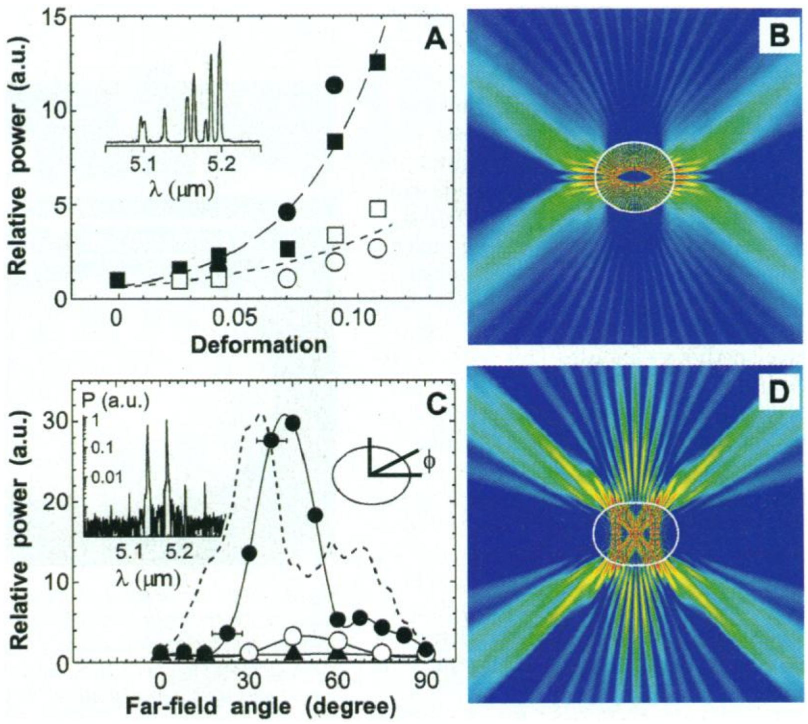

Fig. 3. (**A**) Peak output power of different lasers as a function of deformation. The power is collected around 0° (open symbols) and 90° (filled symbols) with a width of the fixed aperture of 15°. Two independent sets of lasers are presented for each orientation of the aperture. Both curves rise approximately exponentially, as indicated by the dashed line-fit (*26*). (**Inset**) Spectrum in linear scale obtained near peak optical power from a cylinder laser with low deformation ($\varepsilon \approx 0.04$). The close mode spacing observed in the spectrum is a result of several lasing whispering-gallery–type modes. The displayed linewidth is limited by the experimental set-up and data acquisition system. (**B**) False-color representation of the radiation intensity pattern of a chaotic whispering-gallery mode for a deformed cylinder with $\varepsilon = 0.06$ and length of the minor axis of 50 μm. Red indicates high intensity, dark blue indicates minimum intensity on a linear intensity scale. The computational technique is explained in the theory section of the main text. (**C**) Symbols indicate the measured angle-resolved far-field pattern (one quadrant) of a circular (▲) and two deformed lasers with $\varepsilon = 0.14$ (○) and $\varepsilon = 0.16$ (●). The measurements presented here have been taken at a constant-current level, at which the (deformed) lasers displayed pure single-mode emission. However, the far-field shows qualitatively the same characteristic directionality at a current level corresponding to peak optical power. The data sets are normalized to the value measured at zero degrees. The data points are connected by splines (solid lines) for clarity. The dashed line is the calculated far-field intensity pattern associated with the bow-tie mode shown in Fig. 3D, averaged over the experimental aperture. The calculation has been scaled to match the peak emission at $\approx 45°$. The exact angular position of this maximum should be sensitive to the precise shape of the boundary near the bow-tie impact points, and we attribute the off-set between the measured and calculated peak positions primarily to the small deviation between our model and the actual shape and some uncertainty in the precise measurement of the angle. Furthermore, at present, we do not fully understand the discrepancy in the intensities of the secondary peak between calculation and experiment. (**Left inset**) Logarithmic plot of the measured spectrum at maximum power (power P versus wavelength λ) of a laser with $\varepsilon \approx 0.16$. Six equally spaced modes, with mode spacing $\Delta\lambda = 40.4$ nm, are observed. This mode separation is in good agreement with the value of 39.5 nm calculated for a bow-tie orbit corresponding to the calculated intensity pattern of Fig. 3D. (**Right inset**) The polar coordinate system is oriented such that $\phi = 0°$ indicates the direction along the elongated (major) axis, and $\phi = 90°$ denotes the direction of the compressed (minor) axis. (**D**) False-color representation of the intensity pattern of a bow-tie-mode for $\varepsilon = 0.15$ and length of the minor axis of 50 μm. The crossover to the asymptotic far-field pattern of Fig. 3C (dashed line) is relatively slow, and certain features such as the modulated intensity at $\phi = 90°$ vanish in the far-field. The linear color scale (red, high intensity; blue, low intensity) is unrelated to the color scale of Fig. 3B.

pared with the major axis. Figure 3A shows the increase of the output power with ε, collected around 0° and 90°. Both curves rise approximately exponentially, as discussed in the previous section, but "faster" for $\phi = 90°$; in this case the exponent is increased by a factor of ≈ 2 with respect to the $\phi = 0°$ case (26).

This observation is consistent with the expected behavior of deformed whispering gallery modes with an average angle of incidence near the critical angle defined by $\sin(\chi_c) = 1/n$, where $n = 3.3$ is the effective refractive index of the laser waveguide. At zero deformation such a mode has a conserved angle of incidence and emits isotropically and uniformly via evanescent leakage from all points at the boundary (neglecting disorder effects, such as surface roughness scattering). However when the boundary is deformed (11), the angle of incidence of a ray associated with a lasing mode fluctuates and (at these deformations) is most likely to collide with the boundary below the critical angle of incidence at or near a location of high curvature ($\phi = 0°$, 180°). Figure 3B shows the calculated intensity pattern (the modulus squared of the electric field) for a typical whispering-gallery mode in a deformed cylinder laser with $\varepsilon = 0.06$ (the calculational technique will be discussed below). The pattern shows clearly the enhanced emission intensity in the near-field in the vicinity of ($\phi = 0°$, 180°). The experiments are sensitive to the far-field intensity distribution, which depends also on the angle of refraction at the points of high curvature. Both the ray and wave calculations discussed below indicate that at this deformation all whispering-gallery modes with high output coupling have a minimum in emission intensity in the far-field around $\phi = 0°$ and enhanced emission between 45° and 90°. The observed experimental intensity pattern has this general trend (Fig. 3A), but a fully angle- and mode-resolved measurement of the far-field pattern and a detailed comparison with theory is difficult because of the generally low optical power and the many modes that contribute to the laser signal in this regime of deformations. (A detailed discussion of the spectral properties is given in the next section.)

At higher deformations ($\varepsilon \geq 0.14$) we detect a much stronger and qualitatively different directionality. Figure 3C shows the actual angle-resolved far-field pattern (one quadrant) of one circular and two deformed lasers. For the laser displayed in Fig. 1, we obtain a power increase by a factor of 30 into an emission angle of $\phi = 42°$ compared with $\phi = 0°$. The angular width of this directional emission is $\approx 23°$. Around 0° we observe a clear minimum of the emission, and a smooth sloping plateau toward 90°.

At these large deformations, a typical ray characterizing a whispering-gallery mode escapes in less than 10 collisions with the boundary as discussed in the theory section. This ray escape is now approximately isotropic and would seem unlikely to lead to the increased emission anisotropy observed experimentally. Because the general ray motion is furthermore highly chaotic in most of the phase space, the only plausible scenario for generating directional emission is for the lasing modes to be associated with the small regions of stable, regular motion that still remain.

For the range of deformations $\varepsilon \approx 0.12$ to 0.23, there exist only two such regions. The first is in the vicinity of the basic diametral orbit running along the minor axis of the resonator. The associated modes are the transverse modes of the stable, curved mirror Fabry-Perot resonator. However, these modes correspond to normal incidence at the boundary and, as such, would result in a peak emission at 90° in the far-field, in marked contrast to the observation. Furthermore, the low reflectivity of the boundary at normal incidence combined with the short length of the minor axis result in a threshold too high for laser action.

The second region is in the vicinity of the stable four-bounce periodic orbit with the shape of a bow-tie in real space. The intensity pattern of a representative bow-tie mode is shown in Fig. 3D. This orbit comes into existence by bifurcation from the diametral orbit at $\varepsilon \approx 0.10$ and has four equal (in absolute value) angles of incidence on the boundary. At $\varepsilon \approx 0.12$ this angle $\chi \approx 12.5°$ and is well below the critical angle, but as the deformation increases to $\varepsilon \approx 0.15$, this angle increases to approximately the critical angle, $\chi_c \approx 17.5°$. This change results in a sufficiently high reflectivity of the boundary to allow for laser action. For ε of 0.125, 0.14, and 0.15, values of the reflectivity of 0.45, 0.59, and 0.72 are calculated, respectively. In fact, this increase in reflectivity with deformation should lead to a reduction of the laser threshold.

When the radiation intensity pattern of a bow-tie mode is averaged according to the experimental conditions, we find reasonable agreement between the experimental and theoretical far-field directionality (Fig. 3C). We conclude that the laser emission at high deformations originates from the newly observed bow-tie modes. The spectral properties of the emission provide further confirmation of this fact, as discussed in the next section.

The bow-tie orbit is just one of several orbits that move around the minor axis in a librational motion (that is without a fixed sense of rotation) as opposed to the rotational motion of conventional whispering gallery orbits. With higher index of refraction or different shape deformations, modes associated with other librational orbits may be relevant to lasing; hence we will refer to the bow-tie as one of a class of "librational" modes.

In general one would expect that the threshold current density J_{th} should have a minimum for $\varepsilon = 0$ (circular case); increase with deformation until $\varepsilon \approx 0.1$, because of the increase in outcoupling loss; and then decrease because of the gradually increasing reflectivity of the bow-tie modes. In the range of $\varepsilon \approx 0.12$ to 0.2, the observed decrease in J_{th} from ≈ 5 to 4 kA·cm^{-2} is consistent with this expectation. However, in the whispering gallery range of deformations $\varepsilon = 0$ to $\varepsilon \approx 0.08$, the measured decrease in J_{th} from ≈ 7 to 6 kA·cm^{-2} is in contrast with the expectations. Several issues complicate the interpretation of the threshold data. First, a finite lateral current spreading resistance effectively reduces the current density toward the edge of the disk outside the contact region. Second, the mode-confinement factor within the active region is expected to be reduced in the outermost parts of the waveguide because of the true 3D nature of the waveguide, increasing locally the threshold current density. Consequently, the actual threshold current density for a given mode depends on its spatial distribution within the resonator. Our experimental J_{th}, on the contrary, is always calculated by dividing the value of the threshold current by the geometrical area of the actual device.

The threshold current density of the QC laser is given by $J_{th} = (\alpha_{wav} + \alpha_{out})/g_\Gamma$, where α_{wav} is the waveguide loss, g_Γ is the average modal gain coefficient, and α_{out} is the outcoupling loss, which strongly depends on the distributed reflectivity of the boundary, which in turn depends strongly on the deformation ε and effective length of the resonator. From the laser threshold and the computed value of g_Γ (6.72×10^{-3} cm·A^{-1}), the quality factor ("Q value") can be calculated as $Q = (2\pi n)/[\lambda(\alpha_{wav} + \alpha_{out})]$, where n is the effective refractive index and λ the wavelength. The above-cited threshold current densities then result in Q values ranging from ≈ 850 to 1500. Waveguide losses are usually dominant in QC lasers as a result of the high doping levels that increase free-carrier absorption. Finally, lowering of the threshold current density will in general also lead to an increase in the maximum output power as a result of the higher available range of drive currents.

Spectral properties. In addition to the increase in output power and directionality, the increasing deformation also affects the spectral properties of the lasers. These observations further confirm the existence of two different regimes, as manifested in the different types of far-field patterns.

At low deformations we obtain a complex, dense modal spectrum. The lasers are multiple-mode starting from threshold, with close mode spacings, and show up to 10 almost equally strong modes at the maximum optical power (Fig. 3A, inset). This close mode spacing cannot be understood from one fundamental set of longitudinal ("azimuthal") whispering-gallery modes only because fitting an integer number of wavelengths along a single closed ray path would result in a regular comb of modes with significantly larger spacings. We therefore attribute the spectrum to the lasing of several different longitudinal ("azimuthal") and transverse ("radial") modes.

At large deformations the lasers are single-mode until approximately twice the threshold current and show at most two to three strong modes at maximum power. The onset of additional modes is accompanied by a kink in the light output–current characteristic; one can be seen in Fig. 2B. The crossover between the two spectrally characteristic regimes again occurs around $\varepsilon \approx 0.12$.

The multiple-mode behavior of the highly deformed lasers is consistent with the emission from bow-tie modes. The logarithmic plot of a spectrum in this regime (Fig. 3C, left inset) reveals six equally spaced modes, with mode spacing $\Delta\lambda$ = 40.4 nm. The expected theoretical value is calculated assuming that adjacent modes

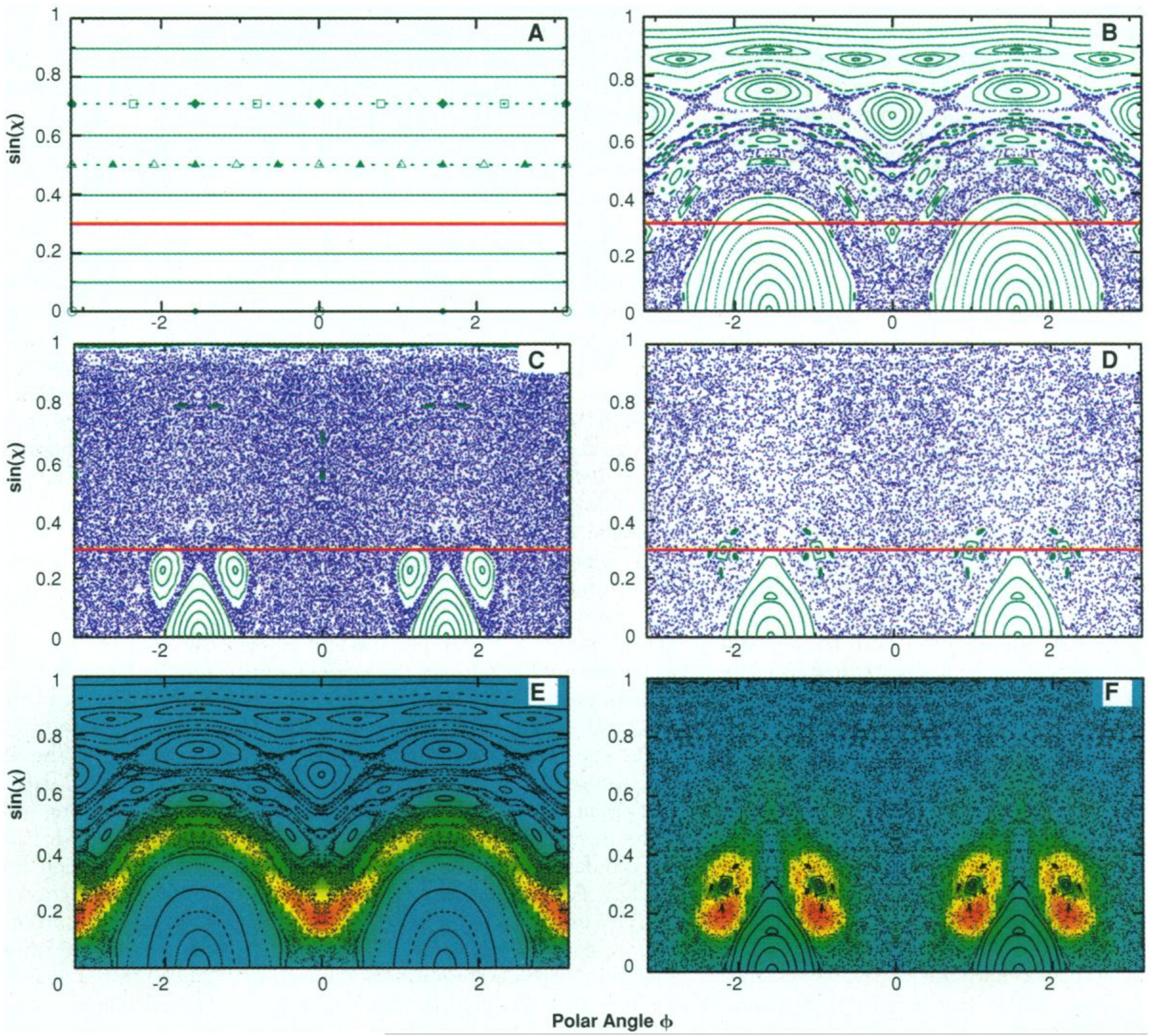

Fig. 4. (A to D) Poincaré surface of section representing the motion of an ensemble of rays in phase space for the flattened quadrupolar billiard, neglecting the possibility of refractive escape. Regions of stable or regular motion are indicated in green, and regions of chaotic motion are indicated in blue. ϕ is the polar angle in radians as defined in Fig. 3C, right inset. (**A**) The undeformed (circular) cylinder. Each trajectory collides with the boundary at a fixed value of the angle of incidence, sin(χ), sometimes closing on itself and forming a periodic orbit, otherwise passing arbitrarily close to any point on the boundary and forming a line in the surface of section. Several members of the infinite families of period-2 (circles), period-3 (triangles), and period-4 (squares, diamonds) orbits are shown. These members survive to nonzero deformation, filled symbols represent orbits that will give stable islands, open symbols those that will be unstable and generate regions of chaos. The red line represents the escape condition, sin(χ) = $1/n$; in the true resonator, rays below that line would rapidly escape by Fresnel refraction. (**B**) The phase space for deformation ε = 0.06, corresponding to the calculation of Fig. 3B. The two major islands at polar angle $\phi = \pm\pi/2$ ($\pm 90°$) correspond to motion around the stable diametral orbit. Just above these islands is the chaotic region generated by the unstable diametral orbit at ϕ = 0, $\pm\pi$ (0, $\pm 180°$). This region contains the chaotic whispering-gallery modes. (**C**) The phase space for ε = 0.125, somewhat after the bifurcation of the diametral orbit (at ε = 0.10) that gives rise to the bow-tie orbits that are seen clearly as the four islands at sin(χ) = 0.22. These islands are sufficiently below the critical line that the corresponding modes would be too short-lived to lase. There are four symmetric islands for negative sin(χ) that are not shown; any one bow-tie orbit only visits four of the islands, two with positive and two with negative sin(χ), but the same path is traced in either case. (**D**) The behavior at ε = 0.15 orresponding to the data and calculation of Fig. 3, C and D. Now the bow-tie islands have moved up to the critical line, increasing the lifetime of the corresponding modes and allowing them to lase. (**E**) Husimi function corresponding to the resonance of Fig. 3B at ε = 0.06; this function clearly represents a chaotic whispering-gallery state localized in the chaotic region. The Husimi function translates the real-space electric field intensity pattern into a probability density in phase space. The resulting function is illustrated by a color scale, where red indicates high intensity. (**F**) The relation between the highly directional resonator mode shown in Fig. 3D and the islands shown in Fig. 4D can be demonstrated by means of the Husimi function shown in Fig. 4F. This function is centered on the bow-tie islands. The minimum at the very center indicates that this bow-tie mode has an oscillatory motion transverse to the bow-tie path; this is consistent with the intensity pattern of Fig. 3D which exhibits four transverse oscillations.

differ by one wavelength along the path length of the bow-tie. This analysis yields a spacing of 39.5 nm, in excellent agreement with the experiment, considering the uncertainty in the effective refractive index.

The bow-tie modes can easily be distinguished from transverse modes of the diametral curved mirror Fabry-Perot resonator along the minor laser axis (length L). As noted above, they originate from a period-doubling bifurcation of the latter, as will be discussed below in greater detail, leading to about twice the optical path length. As such, the bow-tie mode spectrum displays about half the mode spacing one would expect of the standard Fabry-Perot modes, $\Delta\lambda = \lambda^2/(2nL) \approx 82$ nm.

In summary, the experimental data show that imposing a flattened quadrupolar deformation onto semiconductor microlasers substantially improves their power output and directionality. In the favorable directions of the far-field, a power increase of up to three orders of magnitude was obtained. This dramatic result could be achieved by exploiting the complex ray dynamics—first for chaotic whispering-gallery modes, then for bow-tie modes—of the deformed resonators. An in-depth theoretical discussion of the subject is given in the next section.

Theory. The intensity patterns shown in Fig. 3, B and D, were obtained by numerical solution of the Helmholtz equation for the TM polarization resonances at $\lambda \approx 5.2$ μm of a deformed dielectric cylinder with the dimensions and index of refraction ($n = 3.3$) corresponding to those of the experimental structures. These solutions are obtained by matching the internal and external electric fields and their derivatives at the surface of the semiconductor, along with the additional constraint that there is no incoming wave from infinity. The latter constraint implies that the wavevector must be complex, with the imaginary part giving the decay rate or Q value of the resonance (*27*).

To obtain a full theoretical understanding of these resonances, it is helpful to divide the problem into two parts. First, we consider the properties of the "bound states" of the system, corresponding to the discrete solutions that would exist if the cavity were completely closed and the electric field were zero outside the cavity. Then, we must understand how these states are altered by the possibility of escape to infinity by refraction.

The first point is precisely the issue of understanding the solutions of the wave equation within a "billiard." This problem corresponds to a resonator with a mirror reflectivity exactly equal to unity. With these "hard-wall" boundary conditions, the Helmholtz wave equation is identical to the Schroedinger equation of quantum mechanics.

When the cross section of the cylinder is deformed from circularity, the wave equation is no longer separable into three 1D differential equations, and the solutions in the plane transverse to the cylinder axis are no longer specified by pairs of quantum numbers (or mode indices).

One can still obtain a numerical solution, that is, by representing the solution in a large basis set of states and diagonalizing the resulting matrix equations. However, if this approach is used alone, it is difficult to extract any physical understanding of the bound states or resonances, now taking into account the electric field outside the resonator. Indeed, the solutions shown in Fig. 3, B and D, were predicted first by a completely different theoretical approach, before they were found by numerical search. This different approach, which has been pioneered in physics (*28–30*) and physical chemistry (*31*) during the past two decades, is to study the short-wavelength limit of the problem (ray optics for the Helmholtz equation, Newtonian mechanics for Schroedinger's equation) and try to develop a systematic understanding with semiclassical methods. The use of semiclassical methods is justified in our system because the wavelength of light in the material ($\approx$1.6 μm) is much smaller than any of the geometric features of the resonators. Moreover, standard perturbation techniques are not applicable because the deformation causes a shift in the resonance frequencies that is large compared with the resonance spacing.

When the optical wave equation is nonseparable, the corresponding ray motion typically exhibits fully or partially chaotic dynamics, just as the classical limit of a nonseparable Schroedinger equation typically gives a chaotic classical mechanics; this subfield has become known as "quantum or wave chaos theory." The stationary states of these so-called "quantum billiards" have been studied extensively in this context. Here we will discuss the ray-optics properties of the billiards corresponding to the laser resonators studied above, with the goal of understanding the crossover between emission from whispering-gallery to bow-tie modes that occurs in this system.

The relevant billiards are smooth deformations of the circular billiard. Initially we neglect the possibility of escape. Rays will simply propagate indefinitely within the billiard, satisfying the law of specular reflection at collisions with the boundary. When the circle is undeformed, angular momentum is conserved in this motion. The angle of incidence, χ, is the same at each collision, and the orbit traces out an annulus bounded by a circular caustic of radius $R\sin(\chi)$, where R is the radius of the circle. The corresponding wave solutions are the ordinary Bessel functions indexed by the angular momentum quantum number.

When the boundary conditions are changed to include refraction, then rays incident with χ greater than the critical value χ_c given by $\sin(\chi_c) = 1/n$ will remain trapped by total internal reflection, whereas rays with $\sin(\chi) \leq 1/n$ will rapidly escape by refraction according to Snell's law.

To illustrate the circular and deformed case in a unified manner, we represent the ray motion in phase space using the surface of section (SOS) method (*30*, *32*), in which every time a ray collides with the boundary both the azimuthal angle (ϕ), at which it hits, and its angle of incidence (χ) with respect to the boundary are recorded. Following an ensemble of a hundred trajectories for 200 bounces then gives a good picture of the global dynamics in phase space.

The generic behavior of smoothly deformed circular billiards in this representation is shown in Fig. 4, where again we neglect the possibility of escape in calculating the SOS. For the circle (Fig. 4A), the SOS is trivial, and each trajectory gives a straight line corresponding to the conserved value of $\sin(\chi)$, except for trajectories with a chord angle (2χ) equal to a rational fraction, p/q, of 2π. Such trajectories will close after q bounces and are referred to as "period-q" orbits. All such orbits in the circle are marginally stable and exist in infinite families corresponding to arbitrary rotations of any one orbit in the family. Several period-2, period-3, and period-4 orbits are indicated in the SOS of Fig. 4A; the period-2 orbits, which are very important in the discussion below, just traverse the diameter of the circle.

In all of the SOSs in Fig. 4 we have indicated in red the horizontal line corresponding to the critical angle, $\sin(\chi_c) = 1/n = 0.30$. Trajectories that fall below that line in the closed billiard will escape from the semiconductor. Trajectories above the line stay "forever" trapped within the resonator [in this approximation, which neglects weak evanescent leakage (tunneling) of photons (*33*)]. When the circle is deformed, the ray dynamics in the billiard undergo a transition to partially chaotic motion. If the deformation is smooth and the curvature of the boundary is always convex, it can be shown rigorously that the phase space still has nonchaotic whispering-gallery modes for values of $\sin(\chi)$ sufficiently close to one (*34*).

The specific form of the deformation is unimportant for the qualitative physics; we use the flattened quadrupolar deformation, which describes well the experiment. One sees the effect of a deformation of $\varepsilon = 0.06$

in Fig. 4B. For $\sin(\chi) > 0.7$, there remain many unbroken (continuous) curves traversing the full surface of section that correspond to whispering-gallery modes that survive only slightly deformed from the circle. These are whispering-gallery orbits of the familiar type, which are confined near the rim of the resonator, have a true caustic, and will circulate in one sense indefinitely. However, one also now sees the signature of isolated stable and unstable periodic orbits in the motion. The deformation destroys the infinite number of periodic orbits in each family and leaves just an equal number of stable and unstable orbits. The stable orbits are surrounded by closed curves ("islands") that indicate the oscillatory motion of nearby trajectories around the stable periodic orbit. The simplest example in Fig. 4B is the two islands around the stable (short) diametral orbit that collides with $\sin(\chi) = 0$ at $\phi = \pm 90°$. The unstable orbits generate regions of chaotic motion near the islands, which correspond to the grainy structureless regions of the SOS. The most visible example in Fig. 4B extends around the period-2 islands, reaching the $\sin(\chi) = 0$ axis at the location of the unstable (long) diametral orbit [which has $\sin(\chi) = 0$ and $\phi = 0, 180°$]. The bow-tie modes that we have focused on in the previous sections would correspond to a four-bounce orbit centered on the diametral orbit around $\phi = \pm 90°$, but no such orbit exists at this low deformation.

To confirm that the relevant resonances at this low deformation are of the whispering-gallery type, one can generate a phase-space representation of the intensity pattern of Fig. 3B, called the Husimi function (*35*). For the resonance with deformation $\varepsilon = 0.06$ shown in Fig. 3B, this function (shown in Fig. 4E) demonstrates that the ray motion corresponding to this state is spread out in the large chaotic region just mentioned. Because the chaotic region extends through $\sin(\chi) = 0$, an orbit in this region of phase space will eventually change its sense of rotation and is not a whispering-gallery orbit in the familiar sense. However, the Husimi function of Fig. 4E does not have support near $\sin(\chi) = 0$, indicating that escape occurs before this reversal of circulation can happen; hence, the corresponding real-space intensity pattern (Fig. 3B) does have a minimum in the center bounded by an approximate caustic. This orbit lies entirely outside the influence of the central diametral orbit and collides with all regions at the boundary, and thus it may reasonably be termed a "chaotic whispering-gallery" orbit.

At a deformation $\varepsilon = 0.10$, the bow-tie orbit appears at a period-doubling bifurcation (*32*) of the stable diametral orbit. In this case, it is a nongeneric period-doubling bifurcation (*36*) in which a new stable orbit of twice the period is born (the "bow-tie"), while simultaneously two new unstable, V-shaped, period-2 orbits ("birds") are born (Fig. 5). Such period-doubling bifurcations are well understood and can be described quantitatively within the general formalism of nonlinear Hamiltonian dynamics (*32*). However, in this case one can also use a more elementary argument from resonator theory. The stable (vertical) diametral orbit supports standard Gaussian Fabry-Perot modes that are too low-Q to lase in this structure, because of the relatively low reflectivity at normal incidence. When the radii of curvature at the two contact points of this orbit become equal to the distance between them (the minor axis L), we reach the confocal condition (*37*) at which marginally stable families of bow-tie and V-shaped orbits, all of length $4L$, come into existence. For the flattened quadrupole this occurs at $\varepsilon = 0.10$. For slightly larger deformations these orbits leave the vicinity of the diametral orbit and do not correspond to small deformations of diametral orbits. Such orbits are not typically discussed in Fabry-Perot theory (*38*). But here, because the boundary creates a full 180° "mirror" with a reflectivity that increases at oblique incidence, the modes associated with the remaining stable bow-tie orbit are higher-Q than the simple Fabry-Perot modes and can lase when the latter do not. Because they require a doubling of the radius of curvature at the minor axis, they do not exist at small deformations.

The SOS for $\varepsilon = 0.125$ shown in Fig. 4C is taken just after the bifurcation of the diametral orbit, showing the emergence of the stable bow-tie, which has the feature that its angle of incidence is the same for all four bounces (see Fig. 4C legend). Howev-

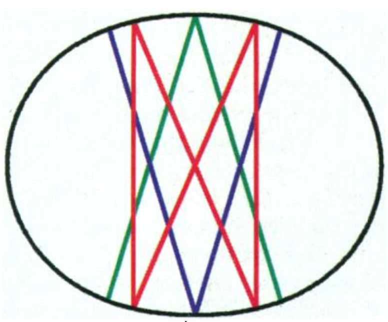

Fig. 5. The three orbits born at the period-doubling bifurcation of the stable diametral orbit, the stable bow-tie (red) and the two unstable V-shaped "birds" (blue, green). The appearance of the orbits occurs at a deformation $\varepsilon = 0.10$. The birds, being unstable, will not generate long-lived resonator modes; however, the stable bow-tie generates modes with directional properties and spectral spacing in excellent agreement with the experiment as discussed above. A key feature of the bow-tie is that it does not exist until the resonator is substantially deformed so that the confocal condition is reached for the stable diametral orbit, as discussed in the text.

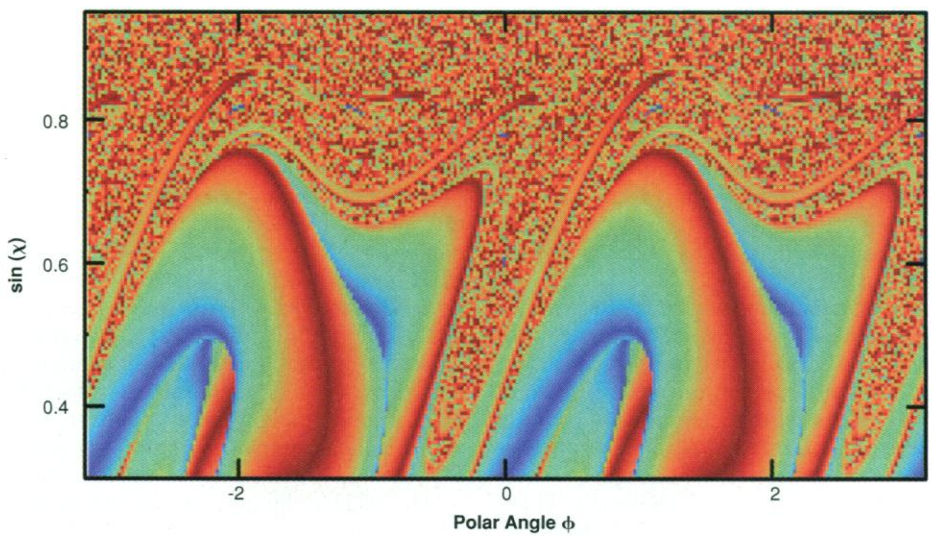

Fig. 6. Color representation of the directionality of escaping rays for the phase space of the flattened quadrupole at $\varepsilon = 0.15$. Initial conditions leading to escape into the far-field at 0° (blue) and at 90° (red) are indicated. A clear demarcation is apparent between a pseudo-random region with rapidly fluctuating escape direction for initial angles $\sin(\chi) > 0.70$ and a regular region where the escape direction varies smoothly and relatively slowly. In the regular region, which primarily corresponds to librational motion, escape is so rapid that chaos cannot fully develop; in contrast, initial conditions in the whispering gallery region above $\sin(\chi) = 0.70$ must traverse more of the chaotic sea and cannot generate highly directional escape. This behavior is completely different from low-index resonators with the same magnitude of deformation (*11*). The regular region can generate directional emission, but only for states localized by islands, such as the bow-tie states.

er, for this deformation, $\sin(\chi) = 0.22$, which is still well below the critical angle.

When the deformation is further increased to $\varepsilon \geq 0.14$, the bow-tie orbit has moved upward in the SOS so that it is centered near the critical angle (Fig. 4D). The reflectivity of the corresponding modes will increase to a value comparable to that of the whispering-gallery modes at the same $\sin(\chi)$ in the circle. Therefore, we expect a turn-on of the laser emission from this mode. The bow-tie orbit now represents the only large stable island at or above the critical angle in the SOS. Moreover, it is now well separated in phase space by a chaotic region from the fundamental diametral orbit from which it originated. The plot in Fig. 3D shows the high-intensity regions concentrated on this orbit. In Fig. 4F, we show the phase-space projection of this mode, which is concentrated in the vicinity of the islands corresponding to the bow-tie orbit.

The modes corresponding to the bow-tie orbit are not simply higher order transverse Fabry-Perot modes; the latter would correspond to quantized oscillations within the island around the diametral orbit. Moreover, as noted above, the bow-tie orbit is rather different from the whispering-gallery orbits because the sense of rotation of the bow-tie orbit is not constant; it represents a librational rather than a rotational motion.

The existence and stability of the bow-tie orbit is relatively insensitive to the precise shape of the boundary, so we expect these modes to be generic to deformed cylindrical resonators. For the flattened quadrupole, the stable bow-tie exists in the range of deformations from $\varepsilon = 0.10$ to $\varepsilon \approx 0.23$. Its directions of peak emission, though, are indeed sensitive to the precise shape of the resonator; the degree of sensitivity will be the subject of future studies (38). Nevertheless, reasonable agreement between theory and experiment has been obtained for the far-field directionality with the flattened quadrupolar shape (Fig. 3C).

As noted above, for the range of deformations at which the stable bow-tie orbit exists, it represents the only substantial islands of stability in the region of phase space close to the critical value of total internal reflection; thus, it is difficult to find a competitive mechanism for the highly directional modes we observe. At lower deformations, other librational modes exist and may be important in the crossover from whispering-gallery to bow-tie emission.

Highly directional emission from low–refractive index resonators was discussed in earlier theoretical work by several of the authors and tested in experiments on lasing dye-jets (*12*). However, the origin of directionality at high deformations in the high–refractive index resonators discussed in the present study is qualitatively different from the mechanism studied in this earlier work. In resonators with indices of refraction $n < 2$, the escape line corresponding to $\sin(\chi) = 1/n$ is much higher in the surface of section. Therefore, a ray escaping from a whispering-gallery mode must traverse a much smaller fraction of the chaotic sea to escape. It has been shown (*11*, *12*) that in this case the motion is not pseudo-random, and highly directional emission from near the points of highest curvature results. However, in the high-index materials of the present work, it is necessary to reach much lower angles of incidence within the resonator to escape, and we now find that the escape direction for rays starting far from the critical angle is indeed effectively random, at least for the deformations where the bow-tie orbit exists. This is demonstrated by the chaotic scattering map shown in Fig. 6. As is explained in the legend to Fig. 6, this map suggests strongly that highly directional modes of the whispering-gallery type are not easily achieved at high deformations in such resonators made from semiconductor materials, although such modes exist and dominate the lasing properties at the same range of deformations for lower index materials. Conversely, modes such as the bow-tie resonance, which are related to librational orbits, all reside well below $\sin(\chi) = 0.5$ and as such would experience too little reflectivity from the boundary to reach laser threshold in low-index materials. The bow-tie modes are confined away from the points of highest curvature in the resonator and thus display a minimum in the near-field intensity at these points (Fig. 3D), in contrast to the whispering gallery modes (Fig. 3B), which have high intensity in the near-field at these points. Therefore, the two types of modes should be easily distinguishable if near-field measurements could be made. This is a demanding task for lasers in the mid-infrared region of the spectrum. Finally, it should be emphasized that there is no fundamental reason that such resonators should not be equally effective as microcavities at visible and near-infrared wavelengths.

REFERENCES AND NOTES

1. Y. Yamamoto and R. E. Slusher, *Phys. Today* **46**, 66 (1993).
2. S. L. McCall, A. F. J. Levi, R. E. Slusher, S. J. Pearton, R. A. Logan, *Appl. Phys. Lett.* **60**, 289 (1991); H. Deng, Q. Deng, D. G. Deppe, *ibid.* **69**, 3120 (1996); T. Baba, *IEEE Select. Top. Quantum Electron.* **3**, 808 (1997).
3. A. F. J. Levi, R. E. Slusher, S. L. McCall, S. J. Pearton, W. S. Hobson, *Appl. Phys. Lett.* **62**, 2021 (1993).
4. S.-X. Qian, J. B. Snow, H.-M. Tzeng, R. K. Chang, *Science* **231**, 486 (1986).
5. H. Yokoyama and K. Ujihara, Eds., *Spontaneous Emission and Laser Oscillation in Microcavities* (CRC, Boca Raton, FL, 1995).
6. M. F. Crommie, C. P. Lutz, D. M. Eigler, *Science* **262**, 218 (1993); C. M. Marcus, A. J. Rimberg, R. M. Westervelt, P. F. Hopkins, A. C. Gossard, *Phys. Rev. Lett.* **69**, 506 (1992).
7. A. Kudrolli, V. Kidambi, S. Sridhar, *Phys. Rev. Lett.* **75**, 822 (1995); H. Alt *et al.*, *ibid.* **74**, 62 (1995); S. Sridhar, *ibid.* **67**, 785 (1991); J. Stein and H. J.Stöckmann, *ibid.* **68**, 2867 (1992); H. D. Gräf *et al.*, *ibid.* **69**, 1296 (1992).
8. A. F. J. Levi *et al.*, *Appl. Phys. Lett.* **62**, 561 (1993); D. Y. Chu *et al.*, *ibid.* **65**, 3167 (1994).
9. B.-J. Li and P.-L. Liu, *IEEE J. Quantum Electron.* 33, 791 (1997).
10. J. Faist *et al.*, *Science* **264**, 553 (1994); F. Capasso, J. Faist, C. Sirtori, A. Y. Cho, *Solid State Commun.* **102**, 231 (1997).
11. J. U. Nöckel and A. D. Stone, *Nature* **385**, 45 (1997).
12. ———, G. Chen, H. Grossman, R. K. Chang, *Opt. Lett.* **21**, 1609 (1996).
13. J. U. Nöckel and A. D. Stone, in *Optical Processes in Microcavities*, R. K. Chang and A. J. Campillo, Eds. (World Scientific, Singapore, 1995), chap.11.
14. ——— and R. K. Chang, *Opt. Lett.* **19**, 1693 (1994).
15. W. T. Silfvast, *Laser Fundamentals* (Cambridge Univ. Press, Cambridge, UK, 1996).
16. H. Liu, S.-H. Zhou, Y. C. Chen, *Opt. Lett.* **23**, 451 (1998).
17. J. Faist *et al.*, *Appl. Phys. Lett.* **69**, 2456 (1996); C. Gmachl *et al.*, *IEEE J. Quantum Electron.* **33**, 1567 (1997).
18. The electric field vector is oriented vertical to the laser plane; therefore, light coupling is prohibited in this direction.
19. J. Faist *et al.*, *Appl. Phys. Lett.* **68**, 3680 (1996); J. Faist *et al.*, *IEEE J. Quantum Electron.* **34**, 336 (1998).
20. The waveguide core contains 25 cascaded stages each consisting of a so-called "three-well vertical transition" active region and an electron injector as described (*19*). The waveguide core is sandwiched between two waveguide cladding layers. Each cladding is composed of three sublayers: a low-doped GaInAs layer (Si doping level $n = 2 \times 10^{17}$ cm^{-3}, thickness $d = 350$ nm) adjacent to the active material; an inner low-doped AlInAs layer ($n = 2 \times 10^{17}$ cm^{-3}, $d = 300$ nm, and $n = 3 \times 10^{17}$ cm^{-3}, $d = 400$ nm); and an outer highly doped AlInAs layer ($n = 7 \times 10^{18}$ cm^{-3}, $d = 1000$ nm), which serves as a plasmon confinement layer (*21*). At the upper cladding hetero-interface between the GaInAs and AlInAs layers, a 2D electron gas (2DEG) (*22*) is formed by highly doping a thin slice ($n = 5 \times 10^{18}$ cm^{-3}, $d = 8$ nm) of the AlInAs layer close to the interface. This together with a highly doped final cap-layer (Sn: $n = 1 \times 10^{20}$ cm^{-3}, $d = 100$ nm) of the structure facilitates lateral current spreading.
21. C. Sirtori *et al.*, *Appl. Phys. Lett.* **66**, 3242 (1995).
22. L. Pfeiffer, E. F. Schubert, K. W. West, *ibid.* **58**, 2258 (1991).
23. The samples are strongly agitated and etched in an aged solution of $HBr:HNO_3:H_2O$ = 1:1:10 for several minutes at room temperature.
24. The rim of the top contact pad has the same distance from the edge of the laser disk (with a small variation of ≈5%) for each laser, in all directions Φ and at all deformations ε. The cylinder lasers have been fabricated with their long diameter oriented in 0°, 45°, and 90° relative to the major orientation of the semiconductor crystal. Finally, the processing leaves the surface clean without evident sources of surface roughness scattering. These precautions ensure that no additional directionality is introduced into the system other than through the flattened quadrupolar shape.
25. The maximum peak power is a widely accepted valid measure of the power performance of semiconductor lasers because it refers to the actual useful power. In the QC laser the peak optical power is reached when the material gain decreases mainly as a result of two effects: the loss of optimum alignment of the ground state of the injector with the upper level of the laser transition with increasing voltage (*39*); and thermal population of the lower laser level with increasing

current density. Therefore the peak power is primarily insensitive to size effects (when normalized to the unit area or volume).
26. There is no strong theoretical basis for an "exponential" power increase, in particular because it is based on several different effects and is far-field dependent. Nevertheless, we chose the term "exponential" increase, because it represents the data qualitatively well.
27. The continuity conditions at the boundary cannot be satisfied for real values of the wavevector if there is no incident wave, so one looks for solutions with complex wavevectors. It can be shown that the real part of these solutions gives the wavevector at which scattering resonances would occur for a wave incident from infinity, whereas the imaginary part gives the width (Q value) of the resonance. In a scattering experiment, the measured intensity in the far-field has contributions both from the resonant scattering and the incident beam, whereas in lasing emission only the resonant emission is present. Hence, it is the intrinsic emission pattern of the quasi-bound state that is measured in the experiments reported, above and it is this quantity that we plot in Fig. 3, B and D. See (*13*), chap. 1, for a detailed discussion.
28. M. V. Berry, *Proc. R. Soc. London Ser. A* **413**, 183 (1987).
29. M. C. Gutzwiller, *Chaos in Classical and Quantum Mechanics* (Springer-Verlag, New York, 1990).
30. L. Reichl, *The Transition to Chaos in Conservative Classical Systems: Quantum Manifestations* (Springer-Verlag, New York, 1992).
31. W. H. Miller, *J. Chem. Phys.* **56**, 38 (1972); P. Gaspard and S. A. Rice, *ibid.* **90**, 2225 (1989).
32. M. V. Berry, *Eur. J. Phys.* **2**, 91 (1981).
33. B. R. Johnson, *J. Opt. Soc. Am.* **10**, 343 (1993).
34. V. F. Lazutkin, *KAM Theory and Semiclassical Approximations to Eigen-functions* (Springer Verlag, Berlin, 1993).
35. The Husimi function is the squared overlap of the interior electric field with a minimum-uncertainty wavepacket centered on a given point in the surface of section. It may be roughly interpreted as a phase-space probability density for the photons in the mode. A precise definition is given in P. LeBoeuf and M. Saraceno, *J. Phys. A Math. Gen.* **23**, 1745 (1990).
36. In a generic period-doubling bifurcation, the shorter orbit becomes unstable as a new stable orbit with twice the period is born. Here, as a result of the symmetry, the shorter (diametral) orbit just reaches marginal stability, the three orbits described in the text are born, and the diametral orbit immediately restabilizes. This is consistent with the Poincaré index theorem because an even number of stable and unstable fixed points are created in this process.
37. B. E. A. Saleh and M. C. Teich, *Fundamentals of Photonics* (Wiley, New York, 1991).
38. We may regard the bow-tie resonances as associated with a four-mirror resonator defined by the tangents to the points of contact of the bow-tie orbit. Some general properties of these modes can be derived from this point of view, which will be presented elsewhere.
39. C. Sirtori *et al.*, *IEEE J. Quantum Electron.*, in press.
40. We are grateful to A. Tredicucci for useful discussions. E.E.N., J.U.N., and A.D.S. gratefully acknowledge support from the Aspen Center for Physics for part of this work. The work performed at Bell Laboratories was supported in part by DARPA (Defense Advance Research Project Agency)–U.S. Army Research Office under contract DAAH04-96-C-0026. The work performed at Yale was supported in part by NSF grant PHY9612200.

23 February 1998; accepted 21 April 1998

Role of the CLOCK Protein in the Mammalian Circadian Mechanism

Nicholas Gekakis,* David Staknis,* Hubert B. Nguyen, Fred C. Davis, Lisa D. Wilsbacher, David P. King, Joseph S. Takahashi, Charles J. Weitz†

The mouse *Clock* gene encodes a bHLH-PAS protein that regulates circadian rhythms and is related to transcription factors that act as heterodimers. Potential partners of CLOCK were isolated in a two-hybrid screen, and one, BMAL1, was coexpressed with CLOCK and PER1 at known circadian clock sites in brain and retina. CLOCK-BMAL1 heterodimers activated transcription from E-box elements, a type of transcription factor–binding site, found adjacent to the mouse *per1* gene and from an identical E-box known to be important for *per* gene expression in *Drosophila.* Mutant CLOCK from the dominant-negative *Clock* allele and BMAL1 formed heterodimers that bound DNA but failed to activate transcription. Thus, CLOCK-BMAL1 heterodimers appear to drive the positive component of *per* transcriptional oscillations, which are thought to underlie circadian rhythmicity.

Circadian clocks are endogenous oscillators that control daily rhythms in physiology and behavior (*1*). Such clocks are phylogenetically widespread (*2*) and are likely to reflect evolutionarily ancient, fundamental mechanisms of timekeeping important for the anticipation of daily variations in environmental conditions (*3*). In mammals, the circadian clock driving metabolic and behavioral rhythms is located in the suprachiasmatic nucleus (SCN) of the hypothalamus (*4*). Mammals and other vertebrates also have an autonomous circadian clock in each retina (*5*) driving rhythms in local physiology that are likely to anticipate the transitions between daytime and nighttime viewing conditions.

The starting point for a molecular analysis of the mammalian circadian mechanism was the identification of a mouse mutant, *Clock*, which has a phenotype affecting both the periodicity and persistence of circadian rhythms (*6*). CLOCK, the predicted protein product of the mutated gene (*7, 8*), is a member of the bHLH-PAS family, some members of which are known to function as transcription factors. The mutant *Clock* allele acts genetically in a dominant-negative fashion (*7, 9*) and encodes a protein with a 51–amino acid deletion in its putative transcriptional regulatory domain (CLOCK-Δ19). How CLOCK controls the periodicity and persistence of circadian rhythms is unknown.

Although not formally demonstrated to encode circadian clock components, three mammalian orthologs of the *Drosophila* clock gene *per*, *mper1* (*10*), *mper2* (*11*), and *mper3* (*12*), have been identified. All three are expressed in the SCN and retina, and, like *Drosophila per*, the levels of their transcripts exhibit a circadian oscillation. Fly and mammalian circadian clocks are thus likely to share a conserved molecular mechanism.

In *Drosophila*, the clock mechanism is constituted in part by a negative feedback loop in which the PER protein directly or indirectly represses transcription of its own gene (*13, 14*). Constitutive *per* mRNA expression has been observed in mutants lacking functional PER protein (*14, 15*), indicating that there is PER-independent positive regulation of *per* transcription. A 69–base pair (bp) "clock control region" located upstream of the *per* gene confers circadian cycling on reporter genes that is dependent on a functional PER protein (*16*). The 69-bp clock control region thus includes sequences sufficient for both PER-dependent negative feedback and PER-independent positive transcriptional regulation. Within this sequence, an E-box element (CACGTG), a binding site for certain transcription factors, is required for the positive component of the transcriptional regulation (*16*).

Precedents for heterodimerization between bHLH-PAS proteins have suggested

N. Gekakis, D. Staknis, H. B. Nguyen, C. J. Weitz, Department of Neurobiology, Harvard Medical School, Boston MA 02115, USA.
F. C. Davis, Department of Biology, Northeastern University, Boston MA 02115, USA.
L. D. Wilsbacher, D. P. King, J. S. Takahashi, Department of Neurobiology and Physiology, Howard Hughes Medical Institute and National Science Foundation Center for Biological Timing, Northwestern University, Evanston, IL 60208, USA.

*These authors contributed equally to this work.
†To whom correspondence should be addressed.